Theor Chem Acc (2013) 132:1375
DOI 10.1007/s00214-013-1375-3

REGULAR ARTICLE

Association reaction between SiH_3 and H_2O_2: a computational study of the reaction mechanism and kinetics

Kaushik Sen · Bhaskar Mondal · Srimanta Pakhira · Chandan Sahu · Deepanwita Ghosh · Abhijit K. Das

Received: 18 January 2013 / Accepted: 24 May 2013

Abstract The association reaction between silyl radical (SiH_3) and H_2O_2 has been studied in detail using high-level composite ab initio CBS-QB3 and G4MP2 methods. The global hybrid meta-GGA M06 and M06-2X density functionals in conjunction with 6-311++G(*d*,*p*) basis set have also been applied. To understand the kinetics, variational transition-state theory calculation is performed on the first association step, and successive unimolecular reactions are subjected to Rice–Ramsperger–Kassel–Marcus calculations to predict the reaction rate constants and product branching ratios. The bimolecular rate constant for SiH_3–H_2O_2 association in the temperature range 250–600 K, $k(T) = 6.89 \times 10^{-13} T^{-0.163} \exp(-0.22/RT)$ cm^3 $molecule^{-1}$ s^{-1} agrees well with the current literature. The OH production channel, which was experimentally found to be a minor one, is confirmed by the rate constants and branching ratios. Also, the correlation between our theoretical work and experimental literature is established. The production of SiO via secondary reactions is calculated to be one of the major reaction channels from highly stabilized adducts. The H-loss pathway, i.e., $SiH_2(OH)_2 + H$, is the major decomposition channel followed by secondary dissociation leading to SiO.

Keywords Silyl radical · Composite ab initio methods · Bimolecular association reaction · VTST · Unimolecular reactions · RRKM · Product branching ratios · Major product channel

Electronic supplementary material The online version of this article (doi:10.1007/s00214-013-1375-3) contains supplementary material, which is available to authorized users.

K. Sen · S. Pakhira · C. Sahu · D. Ghosh · A. K. Das (✉)
Department of Spectroscopy, Indian Association for the Cultivation of Science, Jadavpur, Kolkata 700032, India
e-mail: spakd@iacs.res.in

K. Sen
e-mail: kaushik.physichem@gmail.com

S. Pakhira
e-mail: srimantacu@yahoo.co.in

C. Sahu
e-mail: csk.iit@gmail.com

D. Ghosh
e-mail: deepanwita.ghosh@gmail.com

B. Mondal
Department of Pure and Applied Chemistry, University of Strathclyde, Glasgow G1 1XL, UK
e-mail: pcbhaskar022@gmail.com

1 Introduction

A great deal of effort has been directed toward understanding the mechanism and kinetics of gaseous silicon hydride oxidation chemistry for decades. It is widely agreed that understanding the oxidation mechanism of gaseous silicon hydride is crucial due to the pyrophoric nature of silane as well as in regard to its relevance in chemical vapor deposition (CVD) of silicon oxide (SiO/SiO_2) films in microelectronics industry [1–5], silane combustion, and explosions [6–22]. Silyl radical (SiH_3) is considered to be the dominant species among the other mono-silicon radicals (SiH_n, $n < 3$) to be generated [1, 23–26] during the primary steps of silane decomposition/combustion and also the most abundant radical responsible for the deposition of high-quality amorphous hydrogenated silicon (*a*-Si:H) thin films [2, 23–25]. Therefore, a significant number of mechanistic and kinetic studies have been carried out for the reaction of this radical with a wide range

Published online: 09 June 2013

of species. Krasnoperov et al. [27] reported the gas-phase rate constant for silyl radical for the first time in 1984, but it was not a satisfactory attempt and thus further investigation is required. Until the pioneering work of Yamada and Hirota in 1986 [28], the direct gas-phase kinetics studies of SiH_3 reactions were seriously hindered. Several experimental and theoretical studies thereafter were conducted to have a comprehensive understanding of the complex chemical processes, often economically important, associated with the reactions of SiH_3 with O_2 [29–37], NO [30, 38, 39], NO_2 [30, 32], SiH_3 [26, 38, 40, 41], HBr [42], and some unsaturated hydrocarbons [41]. Recently, Raghunath et al. [43] have extensively investigated the gas-phase mechanism and kinetics of reactions of SiH_3 with SiH_4 and its higher analogue, Si_mH_{2m+2} ($m = 1$–4), with the aid of ab initio and transition-state theory (TST). The reactions of SiH_3 radical are therefore of considerable interest to the researchers.

In the present work, we have elucidated the detailed mechanism and kinetics of much debated gaseous silicon hydride oxidation reaction, taking H_2O_2 as an oxidant, employing density functional theory, high-level composite methods, and theoretical kinetics techniques. Though there are numerous studies, both experimental and theoretical, for the reaction of SiH_3 with O_2 as an oxidant, the role of H_2O_2 as a possible oxidant is relatively ignored. To the best of our knowledge, there is only one experimental investigation available for the reaction of SiH_3 with H_2O_2 in which Meyer et al. [44] have performed a direct measurement of the kinetics, thereby predicting the total rate constant of the title reaction for the first time. Roland et al. [45] roughly estimated the rate constant for the $SiH_3 + H_2O_2$ reaction using an elementary model called independent sheet simulation of photochemical vapor deposition. But there is no theoretical or computational attempt made so far to explore the reaction of SiH_3 with H_2O_2. As an oxidative agent, H_2O_2 is superior to O_2, as the oxidizing capacity of the former is much higher than the later [46]. Furthermore, it has been observed that in the presence of H_2O_2, depletion of SiH_4 is essentially complete [45] and the use of H_2O_2 accelerates the rate of deposition of silicon oxide significantly compared to O_2 [46]. Therefore, in view of the importance of the $SiH_3 + H_2O_2$ reaction for industrial benefit and paucity of experimental and theoretical explorations, careful investigation is necessary in order to understand and accurately model the title reaction and hence the present effort.

The reaction of SiH_3 with H_2O_2 has three possible product channels as postulated by Meyer and Hershberger in their time-resolved infrared diode laser absorption spectroscopic study.

$$\begin{aligned} SiH_3 + H_2O_2 &\rightarrow SiH_2O + OH + H_2 \quad \text{R1} \\ &\rightarrow SiH_4 + HO_2 \quad \text{R2} \\ &\rightarrow SiH_3O + H_2O \quad \text{R3} \end{aligned}$$

But in conclusion, they could not be able to identify the major product channel which still remains a mystery. They also concluded through a branching ratio analysis that the OH producing channel is "less important" than it was believed to be. Their conclusion finds support from the work of Roland et al. [45] where they speculated from the decreasing trend of the ratio of the calculated to the experimental deposition rates that a more oxidized silicon species (SiO_xH_y) is responsible for the film deposition rather than SiH_2O.

The objective of our present study is to explore the complete reaction features theoretically, providing more strong support to the "less important" OH production channel and to search for the existence of any unidentified lower energy reaction channel(s) leading to SiO/SiO_2 production. So, this article is aimed at correlating our theoretical results with the available experimental findings in order to solve the mystery of the major product channels.

We explored the total potential energy surface (PES) for the title reaction using high-level composite methods like CBS-QB3 and G4MP2. As there are a few experimentally obtained heats of formation values for the species involved in the reaction, which are essential for kinetic modeling, we report here the CBS-QB3 and G4MP2 heats of formation values for all the species, which, we believe, would enrich the existing literature. The total rate constant for the $SiH_3 + H_2O_2$ association reaction is evaluated using variational transition-state theory (VTST). Additionally, we performed Rice–Ramsperger–Kassel–Marcus (RRKM) master equation simulation to obtain channel-specific rate constants resulting from the decomposition of primary higher energy adducts. A branching ratio analysis is also performed to identify the major decomposition channels.

2 Computational details

Equilibrium structures of the reactants, products, intermediates, and transition states associated with several processes on PES have been optimized employing density functional theory (DFT) with global hybrid meta-GGA M06 [47] and M06-2X [47] density functionals in conjunction with the triple-ζ quality 6-311++G(d,p) [49] basis set with polarization, and diffusion functions on all atoms. The M06 family of local (M06-L) and hybrid (M06, M06-2X) meta-GGA functionals, developed by Zhao and Truhlar, show promising performance for neutral and radical isomerization/dissociation reaction dynamics. A high

percentage of HF exchange is incorporated with the M06 and M06-2X hybrid meta-DFT methods. Both the functionals considered here are reported to produce excellent results for reaction kinetics. The G4MP2 [50] and CBS-QB3 [51] composite methods are used to obtain more reliable energies of the species, which can be utilized to calculate thermodynamic parameters very accurately. The G4MP2 and CBS-QB3 methods also show a good compromise between computational cost and accuracy. The CBS-QB3 method uses B3LYP/CBSB7 geometries and vibrational frequencies with appropriate scaling for accurate single-point energy calculations. The frequencies used in CBS-QB3 method are scaled by a factor of 0.99. The G4MP2 method uses geometry optimized at the B3LYP/6-31G(2*df*,*p*) level. The zero-point vibrational energy is obtained from vibrational frequency calculation at the same level and the frequencies are scaled by a factor of 0.9854. The potential energy surfaces for the title reaction are constructed using the G4MP2 relative energies, and to analyze the PES and reaction energetics, G4MP2 energies in kcal/mol are used throughout. The connecting first-order saddle points that are the transition states between the equilibrium geometries are obtained using synchronous transit-guided quasi-Newton (STQN) method. Normal-mode analysis has been carried out at the same level of theories for equilibrium as well as transition-state geometries, which are characterized as minima (number of imaginary frequencies NIMAG = 0) or as a transition state (NIMAG = 1). The intrinsic reaction coordinate (IRC) [52, 53] calculations are carried out to validate all connections between transition states and local minima. Minimum energy pathways (MEP) for the association of SiH_3 with H_2O_2 is calculated using relaxed potential energy scan by varying the $O(H_2O_2)$–$Si(SiH_3)$ distance at the B2PLYPD [48]/6-311++G(*d*,*p*) level of theory. All electronic structure calculations are performed with Gaussian 09 suite of quantum chemistry program [54].

The enthalpies of formation at 298 K ($\Delta_fH_{298}^\circ$) for all the species involved in the title reaction are calculated through the atomization scheme [55] using CBS-QB3 as well as G4MP2 electronic energies. For this purpose, we have used the literature values of $\Delta_fH_{298}^\circ$ for Si (107.55 kcal/mol), H (52.10 kcal/mol), and O (59.56 kcal/mol) [56]. Standard entropies (S°) and heat capacities (C_v) are also evaluated using M06-2X/6-311++G (*d*,*p*) energy values at 298 K for all species and transition states.

Variational transition-state theory (VTST) has been employed to compute the rate constants for the barrier-less $SiH_3 + H_2O_2$ association reaction. The VTST allows us to account for the temperature effects on the reaction rates better than the conventional transition-state theory (CTST), as it considers the variation of transition states with temperature on the Gibbs free-energy hypersurface. In VTST approach, the structure-dependent rate coefficients are calculated for different transition-state structures using the transition-state theory (TST) as implemented in the TheRate program [57]. The rate constants are minimized as a function of position along the minimum energy path (MEP) to get the variational rate constant at each temperature. All investigated structures on the MEP contain a single imaginary frequency with the mode vibration corresponding to the motion along the bond-breaking coordinate. This particular approach was successfully employed for a number of barrier-less reactions [58–60].

Apparent rate parameters for the unimolecular decomposition and isomerization of the chemically activated species in the $SiH_3 + H_2O_2$ reaction mechanism are determined using the RRKM [61–64] theory with a time-dependent solution of the master equation, as implemented in the ChemRate code [65]. An exponential down model is used for collision energy transfer with $\langle\Delta E_{down}\rangle = 200\ cm^{-1}$ (0.6 kcal mol^{-1}), where SF_6 is used as a buffer gas. For the reactions that predominantly involve an intramolecular hydrogen shift, rate constants are corrected for quantum mechanical tunneling using Eckart's tunneling correction [66]. We have calculated the barrier width (in $amu^{0.5}$ Å) along the reaction coordinate by fitting the IRC curves with one-dimensional Eckart's potential $V(x)$.

$$V(x) = \frac{e^u}{1+e^u}\left(A + \frac{B}{1+e^u}\right)$$

where $u = 2\pi x/l$, $A = E_1 - E_{-1}$, and $B = E_1^{1/2} + E_{-1}^{1/2}$. x is a coordinate along the reaction path, l is a parameter determining the width of the barrier, and the constants E_1 and E_{-1} represent the barrier heights relative to the reactants and products, respectively. The hindered rotation barriers, as found in some of the species due to O–O, O–Si, O–H rotations, are calculated from a relaxed potential energy surface scan at M062X/6-311 ++G(*d*,*p*) level of theory and are used in RRKM calculations. ChemRate determines moments of inertia for internal rotors based upon molecular structure and connectivity, and these are subsequently employed in evaluating the contribution of the internal rotor to the partition function of the molecule. The calculated rate constants at different pressures are fitted to a modified form of the Arrhenius expression $k = AT^n \exp(-E_a/RT)$, and the Arrhenius parameters A, n, and E_a are calculated for all reaction channels.

3 Results and discussions

3.1 Reaction mechanism

Optimized electronic structures for all the reactants, intermediates, transition states (TS), and products are depicted in

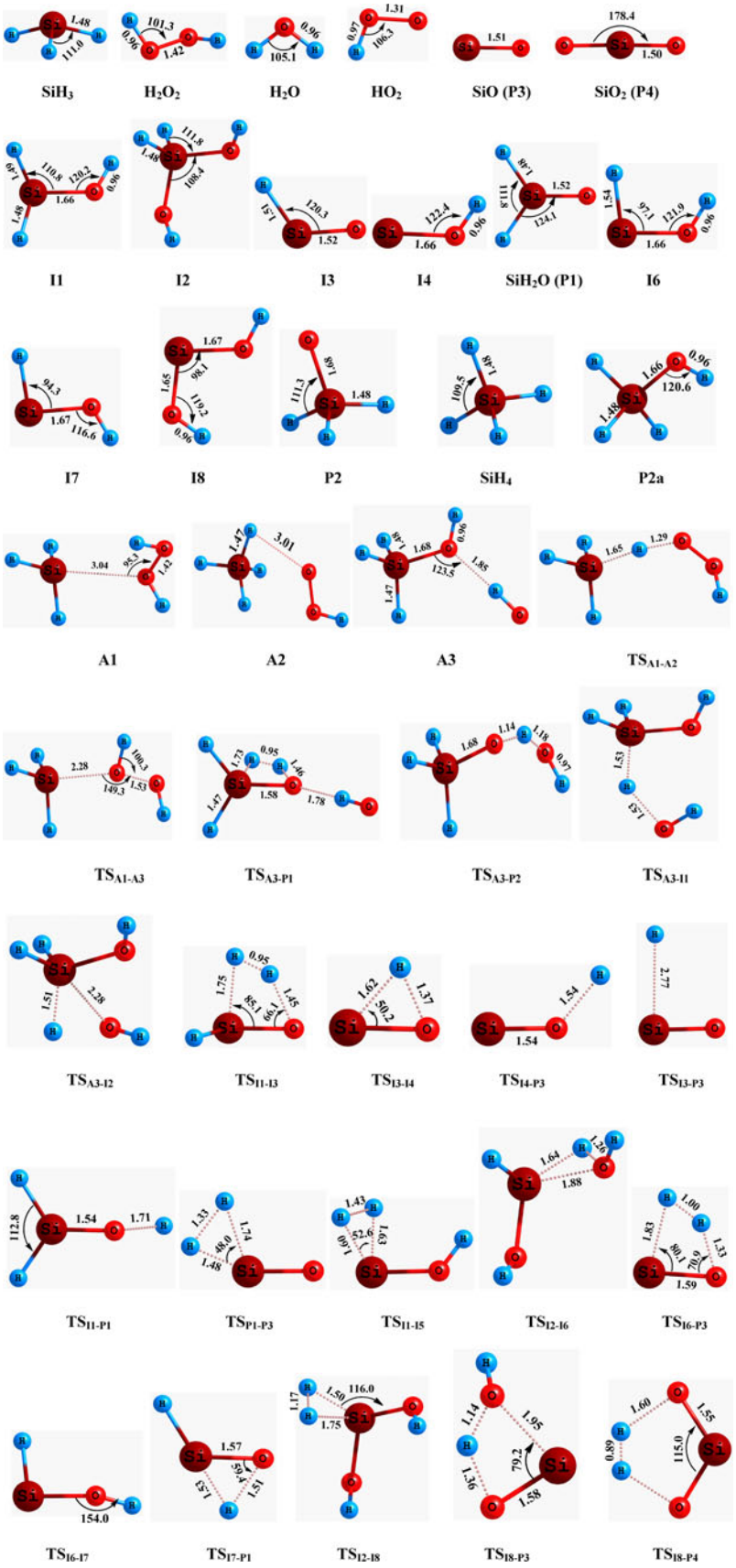

Fig. 1 Optimized geometries with geometrical parameters calculated at the M06-2X/6-311 ++G(*d*,*p*) level for the species involved in the title reaction

Fig. 1 with their optimized geometrical parameters at M06-2X/6-311 ++G (*d*,*p*) level of theory. The global potential energy surfaces (PES) are constructed using the zero-point-corrected relative energies calculated at G4MP2 level of theory. The suitability of these formalisms to treat the present reaction systems has been assessed employing T1 diagnostic test, which is an approximate measure of multireference character in the wave function. It has been suggested that a value in excess of 0.02 for the T1 diagnostic for a closed-shell species indicates that the species in question has significant multireference character [67]. In case of open-shell species, it has been shown [68–73] that T1 diagnostic values up to ~0.045 may be acceptable. In our systems, the T1 diagnostic values for both open- and closed-shell species especially in the TS and MEP calculations are found to be well below the limiting value and expected not to possess significant multireference character. So, the single-reference methods can be applied reliably to characterize the present reaction systems. An inspection of the $<S^2>$ values of the systems also supports this conclusion.

For the sake of convenient presentation and discussion, the total reaction PES is divided into three parts, PES-I, PES-II, and PES-III, which are shown in Figs. 2, 3 and 4, respectively. Unless otherwise stated, the systems with even electrons are in the singlet states, and ones with odd electrons are in the doublet states. For the current systems, PES-I and II are in doublet surface, whereas PES-III is in singlet surface. The total reaction pathway investigated in the present study is shown in Scheme 1. The combined potential energy surface is presented in Fig. S1 in the supplementary material for further reference.

It should be noted here that the complete fragmentation of each species on the PESs is shown in Table 1 and only partial fragmentation is displayed in the Figures to maintain good clarity and readability. Hence, readers are suggested to consult with Table 1 while studying the PESs in the above-mentioned figures. For all PESs, relative energies are calculated with respect to $SiH_3 + H_2O_2$ (**R**) reactant system and presented on PESs in kcal/mol. Energies at different theoretical levels for all species relative to

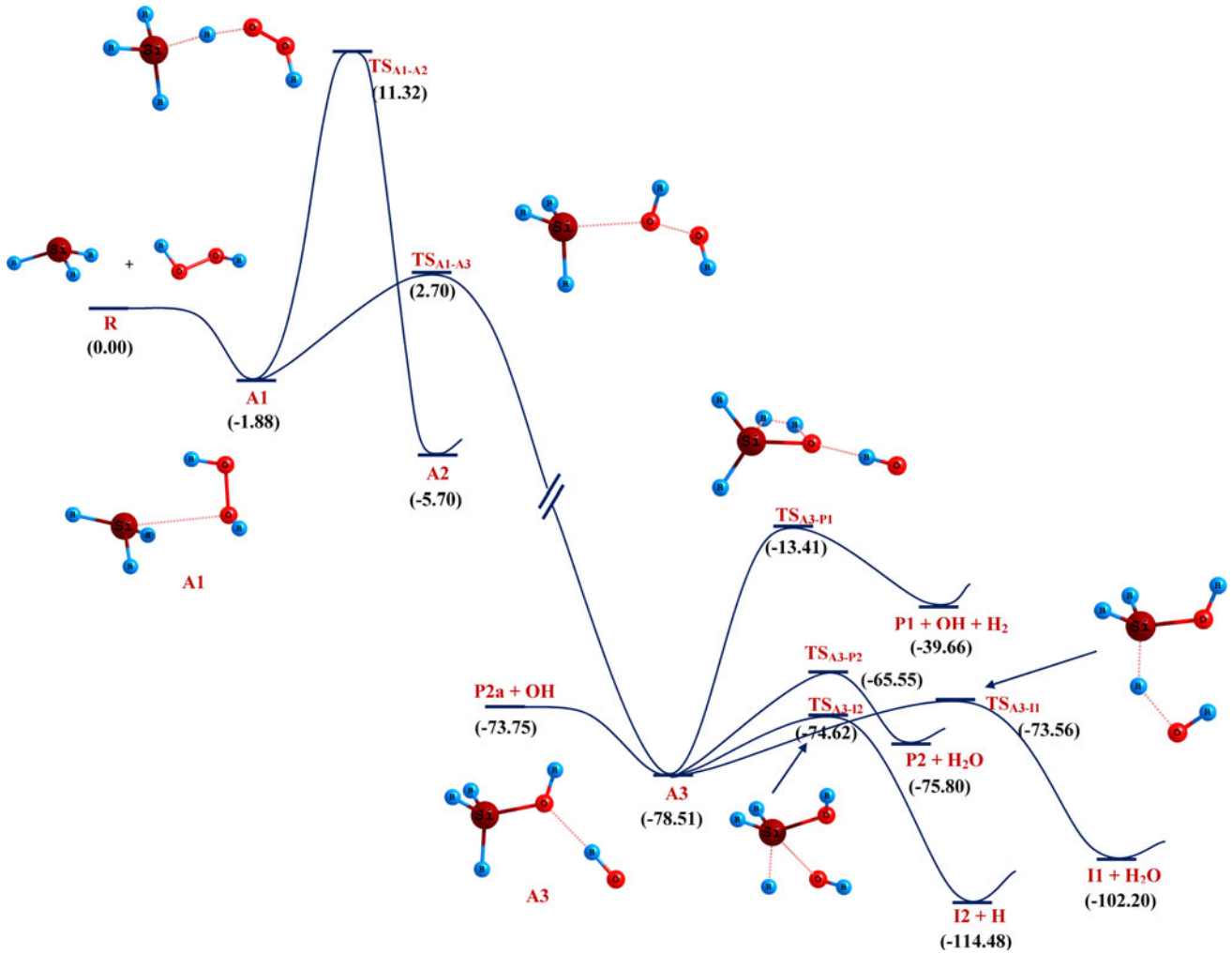

Fig. 2 G4MP2 potential energy surface for the title reaction (**PES-I**)

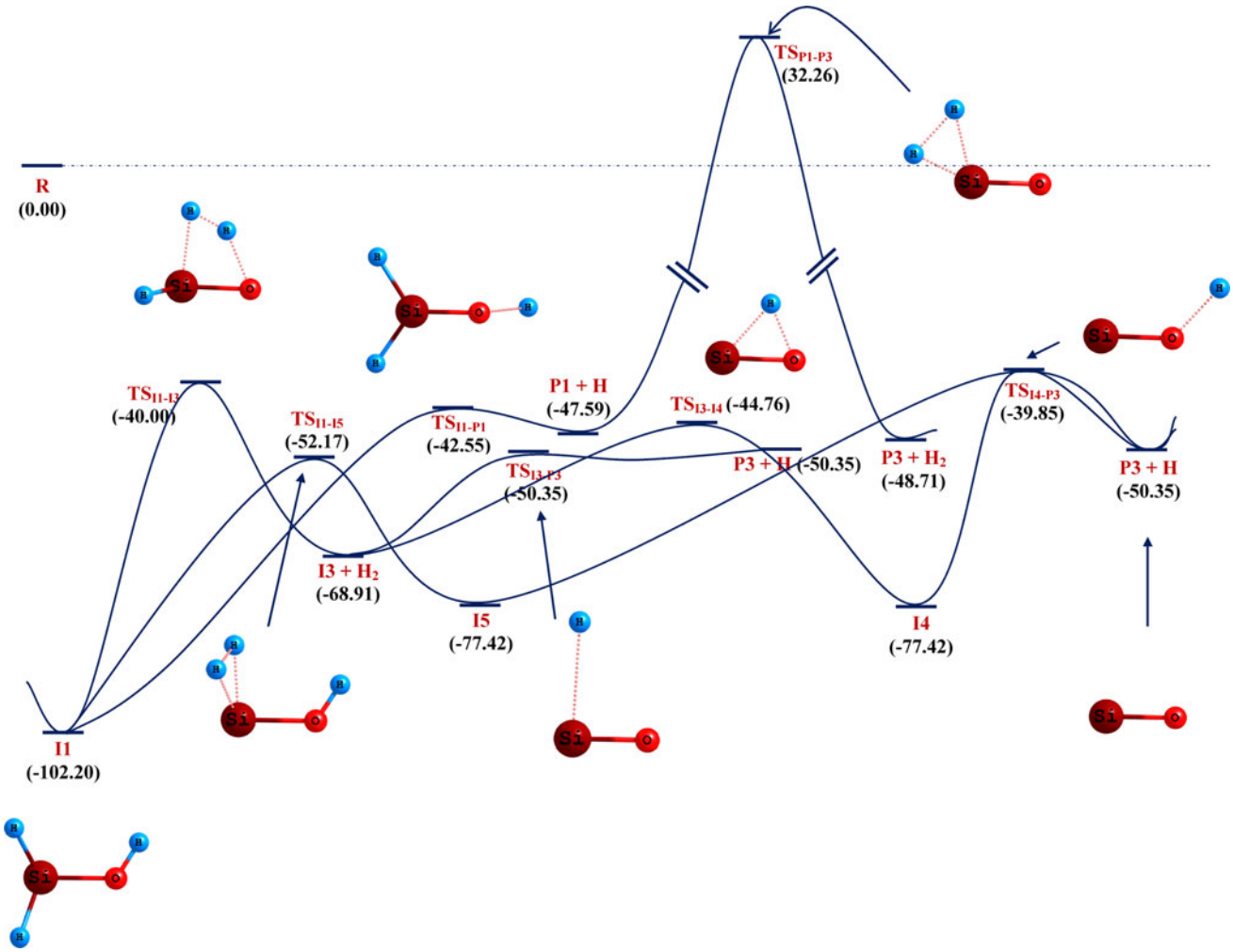

Fig. 3 G4MP2 potential energy surface for the title reaction (**PES-II**)

R are collected in Table 1. The relative energies obtained by density functional theory and composite methods are found to be consistent. In the following discussions of reaction mechanism, we have used G4MP2 relative energies and M06-2X/6-311 ++G(*d*,*p*) geometrical parameters, unless otherwise mentioned.

3.2 PES-I, association reaction of SiH_3 with H_2O_2 and consecutive unimolecular reactions

PES-I is presented in Fig. 2 along with the transition states for each transformation. The association reaction, $SiH_3 + H_2O_2$, proceeds through a nucleophilic attack of the H_2O_2 at the Si center of SiH_3 to form a pre-reaction adduct, **A1** ($SiH_3\cdots H_2O_2$). From an electronic view, the formation of **A1** takes place through an overlap of the lone pair of one oxygen atom (from H_2O_2) on the vacant *d* orbital of Si (from SiH_3). The association reaction is found to be barrier less, and formation of **A1** is exothermic by 1.88 kcal/mol. The weakly bound complex **A1** holds Si–O distance 3.04 Å, and there is no elongation of the O–O distance (1.42 Å) in H_2O_2 on complexation. Now, **A1** can rearrange and transform into **A2** ($SiH_4\cdots OOH$) and **A3** ($SiH_3OH\cdots OH$) through two different exothermic pathways.

3.2.1 *Rearrangement of A1 to $SiH_4\cdots OOH$ (A2)*

A1 can isomerize to a more stable isomer of $SiH_4\cdots OOH$ (**A2**) skeleton through an H-transfer transition state (**TS$_{A1-A2}$**) in which the movement of the transferring H-atom, which is 1.29 and 1.65 Å away from O and Si atoms, respectively, is responsible for the transition vector associated with the imaginary frequency $1624i$ cm^{-1}. The complex **A2** holds the Si–O distance 3.07 Å, which is slightly larger than that we found in **A1**. **A2** contains maximum excess energy of 5.70 kcal/mol but its formation has an energy barrier of 11.32 kcal/mol, which is 8.62 kcal/mol higher compared to the **A3** ($SiH_3OH\cdots OH$) formation. Therefore, **A3** formation is expected to be

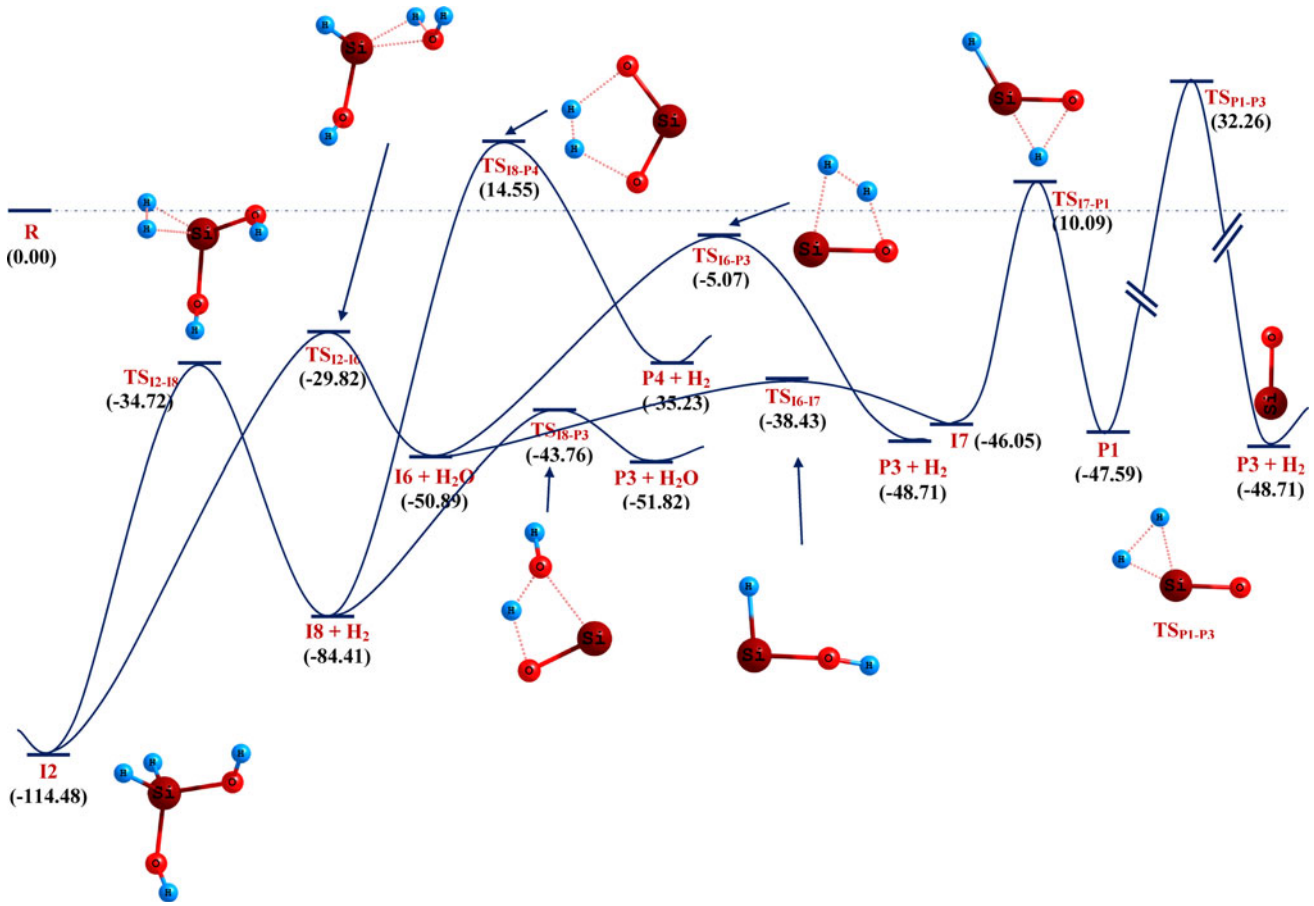

Fig. 4 G4MP2 potential energy surface for the title reaction (**PES-III**)

Scheme 1 Total reaction pathway presented in three separate schemes

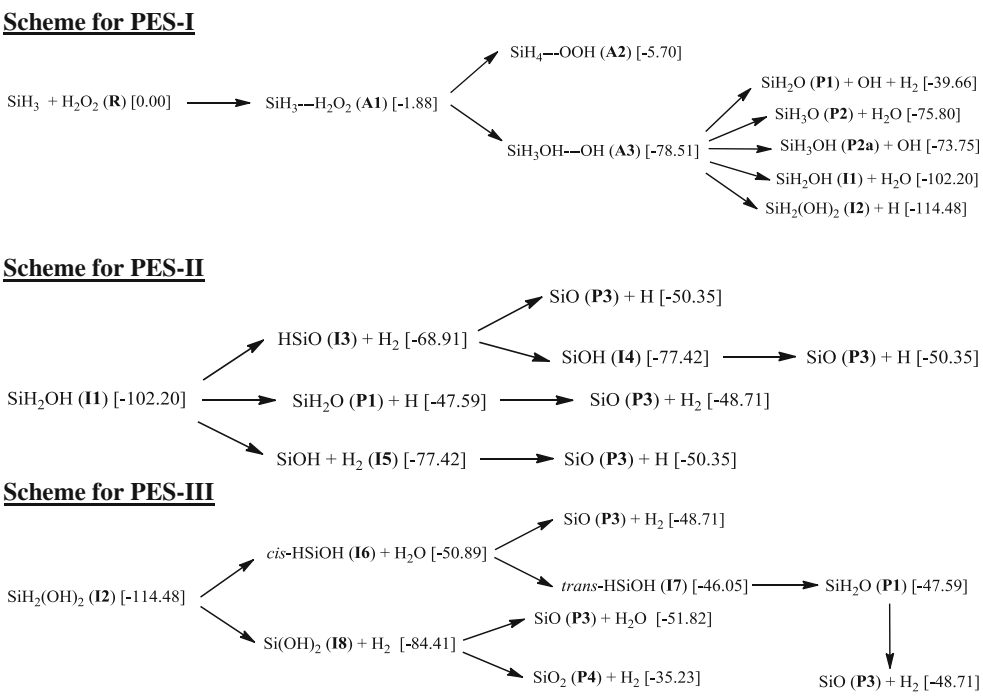

Table 1 Relative energies (kcal/mol) calculated at different theoretical levels for the species involved in the title reaction

Species	M06/6-311 ++G(*d*,*p*)	M06-2X/6-311 ++G(*d*,*p*)	CBS-QB3	G4MP2
PES-I				
$SiH_3 + H_2O_2$ (R)	0.00	0.00	0.00	0.00
A1	−1.98	−2.19	−1.29	−1.88
A2	−7.99	−4.63	−5.25	−5.70
A3	−77.18	−75.13	−76.89	−78.51
I1 + H_2O	−100.00	−100.91	−100.92	−102.20
I2 + H	−105.12	−105.12	−112.24	−114.48
P1 + OH + H_2	−33.18	−31.59	−37.99	−39.66
P2 + H_2O	−78.77	−74.83	−74.68	−75.80
P2a + OH	−72.25	−70.02	−73.15	−73.75
$TS_{A1–A2}$	7.26	10.89	10.51	11.32
$TS_{A1–A3}$	−0.60	2.88	1.73	2.70
$TS_{A3–P1}$	−12.02	−8.30	−13.64	−13.41
$TS_{A3–P2}$	−70.66	−65.01	−66.21	−65.55
$TS_{A3–I1}$	−75.25	−70.75	−72.78	−73.56
$TS_{A3–I2}$	−74.80	−69.59	−73.43	−74.62
PES-II				
I1 + H_2O	−100.00	−100.91	−100.92	−102.20
I3 + H_2 + H_2O	−58.87	−57.96	−67.64	−68.91
P1 + H_2O + H	−41.93	−37.43	−45.67	−47.59
I5 + H_2 + H_2O	−70.39	−72.89	−75.09	−77.42
P3 + H_2 + H_2O + H	−37.67	−38.28	−47.19	−48.71
P3 + H + H_2 + H_2O	−40.05	−40.02	−47.23	−50.35
$TS_{I1–I3}$ + H_2O	−34.73	−32.22	−39.08	−40.00
TS_{I3-I4} + H_2 + H_2O	−30.10	−36.27	−42.59	−44.76
$TS_{I4–P3}$ + H_2 + H_2O	−31.39	−31.33	−36.90	−39.85
$TS_{I3–P3}$ + H_2 + H_2O	−38.98	−39.18	−47.24	−50.35
$TS_{I1–P1}$ + H_2O	−36.79	−32.80	−40.57	−42.55
$TS_{P1–P3}$ + H_2O + H	38.81	44.26	33.98	32.26
$TS_{I1–I5}$ + H_2O	−49.09	−47.85	−50.64	−52.17
PES-III				
I2 + H	−105.12	−105.12	−112.24	−114.48
I6 + H_2O + H	−51.15	−50.10	−49.71	−50.89
I7 + H_2O + H	−43.48	−42.27	−44.58	−46.05
P1 + H_2O + H	−41.93	−37.43	−45.67	−47.59
I8 + H_2 + H	−73.74	−78.48	−82.82	−84.41
P3 + H_2O + H_2 + H	−46.89	−47.14	−51.21	−51.82
P4 + H_2 + H_2 + H	−20.64	−18.82	−34.76	−35.23
P3 + H_2 + H_2O + H	−37.67	−38.28	−47.19	−48.71
$TS_{I2–I6}$ + H	−26.65	−26.19	−28.79	−29.82
$TS_{I6–P3}$ + H_2O + H	−0.47	1.44	−3.99	−5.07
$TS_{I6–I7}$ + H_2O + H	−37.25	−35.77	−36.84	−38.43
$TS_{I7–P1}$ + H_2O + H	16.03	20.85	11.56	10.09
$TS_{P1–P3}$ + H_2O + H	38.81	44.26	33.98	32.26
$TS_{I2–I8}$ + H	−26.13	−25.09	−33.03	−34.72
$TS_{I8–P3}$ + H_2 + H	−36.93	−38.93	−42.54	−43.76
$TS_{I8–P4}$ + H_2 + H	31.16	35.82	16.91	14.55

exclusive and we have explored all possible channel(s) originating from **A3**.

3.2.2 Rearrangement of A1 to $SiH_3OH\cdots OH$ (A3)

A1 can isomerize in a different way to form another complex **A3** ($SiH_3OH\cdots OH$) which contains maximum excess energy of 78.51 kcal/mol. The formation of **A3** is extremely exothermic by 76.63 kcal/mol (relative to **A1**), which is about 73 kcal/mol more exothermic than that of **A2**. The formation of **A3** involves the rupture of the O–O bond and simultaneous formation of the Si–O bond through a transition state, $\mathbf{TS_{A1-A3}}$, which is 2.70 kcal/mol above the reactants, **R**. In $\mathbf{TS_{A1-A3}}$, the Si–O distance is shortened by 0.76 Å and the O–O distance is elongated by 0.11 Å relative to the primary complex, **A1**. **A3** formed in this way holds a Si–O distance of 1.68 Å. Now, from thermodynamic as well as kinetic point of views, we can easily discard the **A2** formation pathway compared to **A3** formation. Since **A3** has an excess energy of 78.51 kcal/mol, it can enter into further irreversible unimolecular decomposition reactions leading to various products and high-energy intermediates. Following the proposal of Meyer et al. [44], we first try to explore the SiH_2O and SiH_3O formation pathways, because the SiH_4 formation pathway is ruled out from energetic and kinetic considerations.

3.2.3 A3 to SiH_2O (P1)

SiH_2O **(P1)** can be produced through a H_2 elimination mechanism from **A3** through $\mathbf{TS_{A3-P1}}$ with an energy barrier of 65.10 kcal/mol. The formation of SiH_2O is a H_2 elimination pathway, and the corresponding TS having an imaginary frequency of 1621*i* is associated with the transition vectors dominated by the motions of the dissociating H-atoms. The OH radical is also formed along with SiH_2O and H_2 through this pathway. The conversion of **A3** to SiH_2O is highly endothermic by 38.85 kcal/mol, making this pathway energetically unfavorable compared to other parallel channels from **A3**. The high activation energy, 65.10 kcal/mol (relative to **A3**), further prevents the formation of SiH_2O along with H_2 and OH compared to other products. Therefore, among several possibilities of unimolecular decomposition pathways from the primary complex, **A3**, the OH formation pathway can be listed as a minor product channel. This observation is consistent with the experimental observation of Meyer et al., where the OH formation was ruled out using product analysis.

3.2.4 A3 to SiH_3O (P2)

Elimination of a water molecule from **A3** leads to the formation of SiH_3O (**P2**) directly through an intramolecular H-transfer reaction. The intramolecular H-transfer transition state, $\mathbf{TS_{A3-P2}}$, possesses 12.96 kcal/mol activation barrier and makes this channel more favorable than SiH_2O (**P1**) formation channel. This water elimination channel is still endothermic by 2.71 kcal/mol, which is much lower than that of the former channel. It may be noted here that the Si–O distance (1.68 Å) does not change along the water elimination pathway.

3.2.5 A3 to SiH_3OH (P2a)

In addition to the four different decomposition channels, **A3** can also decompose directly to give SiH_3OH (**P2a**) and OH, which occurs through barrier-less process with an endothermicity of 4.76 kcal/mol above **A3**. This direct decomposition channel is calculated to be highly exothermic by 73.75 kcal/mol relative to the reactant **R**, but high exothermicity of SiH_2OH (**I1**) and $SiH_2(OH)_2$ (**I2**) formation channels are expected to diminish the formation of **P2a** and therefore OH.

3.2.6 A3 to SiH_2OH (I1)

Here, we evaluate a water elimination pathway from **A3**, which leads to the formation of SiH_2OH (**I1**). The water elimination mechanism featuring H-abstraction from Si–H bond by OH is found to be operative during the formation of **I1** from **A3** through $\mathbf{TS_{A3-I1}}$. This process is associated with an activation barrier of only 4.95 kcal/mol, which is significantly lower than the pathways discussed above and therefore kinetically favored. The ejection of H from Si center is favored due to the lower bond strength of the Si–H bond. $\mathbf{TS_{A3-I1}}$ possesses an imaginary frequency of 1003*i* due to the transition vector governed by the movement of the transferring H-atom. The transferring H-atom is equidistant (1.53 Å) from Si and O atoms in the TS. This conversion is significantly exothermic by 23.69 kcal/mol, making it thermodynamically favored over the above two pathways. Therefore, our assumption toward the formation of SiH_2OH leads to a kinetically and energetically favorable decomposition channel from **A3**.

3.2.7 A3 to $SiH_2(OH)_2$ (I2)

We also paid our major attention to the formation of $SiH_2(OH)_2$ **(I2)** from **A3** through a single pathway with loss of hydrogen. The reaction is found to pass through a transition state, $\mathbf{TS_{A3-I2}}$, in which the dissociating H-atom is 1.51 Å away from Si atom. The conversion of **A3** to $SiH_2(OH)_2$ (**I2**) has a barrier height of only 3.89 kcal/mol, which is comparable with the previous SiH_2OH (**I1**) formation channel. The small barrier and exothermicity of 35.97 kcal/mol make the channel favorable. We identify

the **I2** formation channel as the favored, kinetically as well as thermodynamically, decomposition channel among all channels from **A3**.

The first two pathways were proposed at the beginning of experimental study [44] and attempts were made to identify the OH radical which was reported to be a minor product, which is supported by our findings also. We modeled the **I1** formation pathway following the work of Tsang et al. and finally we propose the **I2** formation pathway which is reported for the first time. The **I1** and **I2** product channels are comparable from kinetic as well as thermodynamic analysis and are the dominant among four possible decomposition pathways. Therefore, we decided to consider further these two channels because they have potential for the formation of silicon oxide (SiO/SiO_2) leading to SiO/SiO_2 deposition during CVD. The identification of major product channel finds support from the simulation study of Roland et al. [45], where they anticipated the presence of a more oxidized silicon species than SiH_2O as the important film precursor. This was also supported by the ab initio study of Murakami et al. [36] and Kondo et al. [34]. Additionally, they found the H-atom producing channel to be dominant for a similar reaction system $SiH_3 + O_2$ rather than the OH producing one. These observations support our results for the favorable decomposition channel from **A3** leading to **I2**.

3.3 PES-II, unimolecular reactions from SiH_2OH (I1)

The possible unimolecular dissociations from SiH_2OH (**I1**) and consecutive reactions have been studied and are presented in PES-II (Fig. 3) along with the TSs for all transformations. We locate three dissociation channels from **I1**, all of them leading to the formation of Si–O through multistep hydride (H) or hydrogen (H_2) elimination pathways. First, we discuss the dissociations channels from **I1**.

3.3.1 SiH_2OH(I1) to SiO via I3

I1 may get dissociated to **I3** (HSiO) through a H_2 elimination mechanism having barrier height of −40.00 kcal/mol (relative to **R**). The H_2 elimination TS, $\mathbf{TS_{I1–I3}}$,—located for this conversion, is a four-member TS having the cleaved H-atoms 1.75 and 1.45 Å away from the Si and O atoms, respectively. The leaving H-atoms are perpendicular to the HSiO plane and the imaginary frequency associated with the H-elimination is 1763*i*. **I3** formed in this way can isomerize to **I4** (SiOH) via H-transfer TS, $\mathbf{TS_{I3–I4}}$, over a barrier height (−44.76 kcal/mol relative to **R**) smaller than the initial dissociation. $\mathbf{TS_{I3–I4}}$ is a triangular TS with Si–H and O–H distances 1.62 and 1.37 Å, respectively. **I4** finally dissociates to SiO (**P3**) via hydride elimination pathway which has a barrier height of −39.85 kcal/mol (relative to **R**). The hydride elimination TS, $\mathbf{TS_{I4–P3}}$, has an imaginary frequency of 1615*i* for hydrogen movement. In parallel, **I3** can also dissociate directly via a hydride elimination pathway to form **P3** through $\mathbf{TS_{I3–P3}}$with a barrier of height −50.35 kcal/mol (relative to **R**), which is 5.59 kcal/mol lower than the former (**I3** → **I4** → **P3**) consecutive pathway.

The formation of SiO from the unimolecular dissociation of **I1** via **I3** is calculated to be favorable, as the associated barrier heights are lower compared to **R**. In particular, **I1** will prefer to dissociate to SiO via **I3** through a single-step hydride elimination pathway rather than a two-step pathway.

3.3.2 SiH_2OH (I1) to SiO via P1

I1 may convert to SiO through consecutive H and H_2 elimination paths. In the first step, H-elimination from **I1** leads to the formation of **P1** (SiH_2O) through TS, $\mathbf{TS_{I1–P1}}$, with a barrier height of −42.55 kcal/mol (relative to **R**). **P1** formed in this way possesses energy of −47.59 kcal/mol relative to **R**. **P1** may then lead to the formation of SiO via H_2 elimination through TS, $\mathbf{TS_{P1–P3}}$, which has energy of 32.26 kcal/mol (relative to **R**). The SiO formed in this way involves barrier heights of −42.55 and +32.26 kcal/mol, between which the final step barrier is high and even higher than the maximum excess energy of **P1** (−47.59 kcal/mol). This process does not seem to be energetically feasible and the formation of SiO through this channel is not important.

3.3.3 SiH_2OH (I1) to SiO via I5

In parallel to above-discussed channels, **I1** may dissociate to SiO through a direct H_2 elimination pathway involving the formation of **I5** (SiOH (**I4**) + $\mathbf{H_2}$). This dissociation passes through $\mathbf{TS_{I1–I5}}$ with a barrier height of −52.17 kcal/mol. The **I5**, in its H_2 eliminated form (i.e., **I4**), connects the final product SiO through the aforementioned TS, $\mathbf{TS_{I4–P3}}$. This SiO formation pathway involves lowest barrier height among three possible pathways (**I1** → **I3** → **P3**, **I1** → **P1** → **P3**, and **I1** → **I5** → **P3**) and dominates over the other favorable channel (SiO via **I3**).

In summary, the stable intermediate **I1** can lead to the formation of SiO through two possible channels (**I1** → **I3** → **P3** and **I1** → **I5** → **P3**) having accessible energy (maximum excess energy for $\mathbf{TS_{I1–I3}}$ is −40.00 kcal/mol and that for $\mathbf{TS_{I1–I5}}$ is −52.17 kcal/mol) and therefore can be considered as a major product channel from the $SiH_3 + H_2O_2$ association forming SiO, H_2, and H. Our observation for this major product channel is consistent with an analogous oxidation reaction of SiH_3 ($SiH_3 + O_2$) [36].

3.4 PES-III, unimolecular reactions from $SiH_2(OH)_2$ (I2)

Now, we consider the possible unimolecular reactions from the most stable reaction intermediate of $SiH_3 + H_2O_2$, **I2**, which has a maximum excess energy of −114.48 kcal/mol. The unimolecular reactions generated from **I2** have been monitored and presented in PES-III (Fig. 4) along with the TSs for all transformations. Our search for the pathways from **I2** decomposition resulted in two dissociation channels, each leading to the formation of SiO. We have also calculated SiO_2 formation from one of the branched channels. Unimolecular H_2O and H_2 elimination reactions initiate the consecutive reactions toward SiO/SiO_2. We consider the dissociation cannels from **I2** in detail below.

3.4.1 $SiH_2(OH)_2$ (I2) to SiO via HSiOH (I6)

I2 may lose a water molecule through an intramolecular H-atom transfer from Si to one O atom with concerted rupture of the Si–O bond leading to the formation of **I6** (HSiOH) + H_2O. The reaction passes through transition state, $\mathbf{TS_{I2–I6}}$, involving a barrier height of −29.82 kcal/mol [relative to **R** (the $SiH_3 + H_2O_2$ entrance channel)]. The $\mathbf{TS_{I2–I6}}$ is a three-member cyclic transition state in which the moving H-atom is 1.64 and 1.26 Å away from the Si and O atoms, respectively. The dissociating Si–O distance increases from 1.65 to 1.88 Å and an imaginary frequency of 1590*i* corresponds to the transition vector for the hydrogen transfer. The *cis*-HSiOH formed in this way can dissociate directly to SiO (**P3**) by the elimination of molecular hydrogen via TS, $\mathbf{TS_{I6–P3}}$, over a barrier height of −5.07 kcal/mol (relative to **R**). In parallel to this dissociation via H_2 elimination, **I6** can undergo isomerization to **I7** (*trans*-HSiOH). This *cis–trans* isomerization has an activation energy of 12.46 kcal/mol (relative to **I6**) and it occurs through the TS, $\mathbf{TS_{I6–I7}}$. This *trans* isomer **I7** (HSiOH) can undergo further rearrangement to form **P1** (SiH_2O) through 1,2 H-transfer via a cyclic TS, $\mathbf{TS_{I7–P1}}$, with barrier height of 10.09 kcal/mol (relative to **R**). Finally, the elimination of molecular hydrogen from **P1** leads to the formation of SiO (**P3**) via $\mathbf{TS_{P1–P3}}$ having activation barrier of 32.26 kcal/mol (relative to **R**). The actual activation energy, 79.85 kcal/mol (relative to **P1**), for this reaction process is consistent with the calculations of Zachariah and Tsang [74]. The formation of SiO in this pathway is clearly unfavorable due to the fact that the barrier heights (10.09 and 32.26 kcal/mol) for the final step are higher (at 298 K) than the maximum excess energy of −50.89 kcal/mol of **I6**. Therefore, **I2** can produce SiO through a two-step consecutive pathway via **I6**.

3.4.2 $SiH_2(OH)_2$ (I2) to SiO/SiO_2 via $Si(OH)_2$ (I8)

Parallel to H_2O elimination in the previous step, **I2** can lose one H_2 through a more kinetically favorable pathway to form **I8** ($Si(OH)_2$). The formation of **I8** involves $\mathbf{TS_{I2–I8}}$ with barrier height of −34.72 kcal/mol (relative to **R**), which is about 5 kcal/mol lower than the above parallel dissociation through H_2O elimination. In $\mathbf{TS_{I2–I8}}$, the departing H-atoms are 1.50 and 1.75 Å away from the associated Si atom, respectively, and the imaginary frequency of 1465*i* accounts for the motions of the leaving H-atoms. **I8** formed in this way can dissociate via H_2O and H_2 eliminations in parallel pathways. The direct elimination of one H_2O from **I8** leads to the formation of SiO (**P3**) with a barrier height of −43.76 kcal/mol (relative to **R**). The TS involved in this transformation ($\mathbf{TS_{I8–P3}}$) is a four-member one with the moving H-atoms at 1.36 and 1.14 Å from the O atoms, respectively, and the dissociating Si–O distance is 1.95 Å. In parallel, a direct elimination of H_2 from **I8** produces SiO_2 (**P4**) through the transition state, $\mathbf{TS_{I8–P4}}$. This SiO_2 formation step involves a barrier height of 14.55 kcal/mol (relative to **R**). The formation of SiO_2 from $SiH_2(OH)_2$ (**I2**) involves a barrier height, which is larger than the maximum excess energy of $Si(OH)_2$ (**I8**) (−84.41 kcal/mol) and therefore unfavorable.

In summary, SiO can be produced from the stable intermediate **I2** of $SiH_3 + H_2O_2$ reaction through two favorable channels, whereas the formation of SiO_2 from **I2** does not seem to be energetically favorable.

3.5 Thermochemistry

The present study demands the calculation of the important thermochemical parameter, the standard enthalpies of formation at 298 K ($\Delta_fH_{298}°$), to understand the formation and stability of all the reactant complexes, intermediates, and products involved in the title reaction. The standard enthalpies of formation at 298 K ($\Delta_fH_{298}°$) are calculated using the atomization scheme [55]. We have calculated $\Delta_fH_{298}°$ accurately using CBS-QB3 and G4MP2 electronic energies for all the species and the results are collected in Table 2. Due to the lack of experimental $\Delta_fH_{298}°$ data for most of the species involved in this study, the efficiencies of the methods are tested by comparing the calculated enthalpy of formation values with the existing literature for SiH_3, H_2O_2, SiH_2O, SiH_4, SiO_2, HSiOH, and SiO and good agreement is found for both of the selected methods (refer to Table 2). Additionally, the $\Delta_fH_{298}°$ values for the transition states involved in the title reaction have also been calculated. The calculated standard enthalpies of formation, presented in Table 2, are used for the kinetics calculation using the ChemRate program. Other thermochemical

Table 2 Enthalpies of formation ($\Delta H_f°$, 298 K) at CBS-QB3 and G4MP2 levels of theory

Species	CBS-QB3	G4MP2	Expt.
SiH_3	45.71	46.30	46.61 ± 1.4[a]
H_2O_2	−33.41	−31.19	−32.53[b]
HO_2	2.24	3.38	0.50[b]
SiH_4	5.38	7.10	8.2[b]
A1	11.24	13.42	
A3	−65.53	−64.24	
I1	−28.54	−27.76	
I2	−151.89	−148.92	
I3	5.11	5.72	
I4	−1.80	−2.12	
I6	−25.02	−24.33	
I7	−25.02	−24.33	−36 ± 10[c]
P1	−26.13	−24.18	−36 ± 10[c]
I8	−120.47	−119.33	
P2	−1.77	−0.87	
P2a	−69.83	−67.37	
P3	−24.97	−24.51	−24.0[b]
P4	−69.48	−67.64	−73.0[b]
$TS_{A1–A2}$	22.13	25.80	
$TS_{A1–A3}$	13.59	17.52	
$TS_{A3–P1}$	−2.10	0.81	
$TS_{A3–P2}$	−55.01	−51.53	
$TS_{A3–I1}$	−61.18	−59.13	
$TS_{A3–I2}$	−62.02	−60.27	
$TS_{I1–I3}$	31.15	32.40	
$TS_{I1–I5}$	19.77	20.41	
$TS_{I1–P1}$	30.25	30.45	
$TS_{I3–P3}$	26.52	25.44	
$TS_{I3–I4}$	30.62	30.48	
$TS_{I4–P3}$	36.47	35.54	
$TS_{I2–I8}$	−72.90	−71.78	
$TS_{I2–I6}$	−68.60	−66.85	
$TS_{I8–P4}$	−20.39	−20.09	
$TS_{I8–P3}$	−79.90	−78.48	
$TS_{I6–P3}$	15.44	16.53	
$TS_{I6–I7}$	−17.05	−16.59	
$TS_{I7–P1}$	31.38	32.04	
$TS_{P1–P3}$	53.59	54.02	

[a] Ref. [75]

[b] Ref. [76]

[c] Ref. [77]

properties ($S°$ and C_v) at 298 K are also calculated using M06-2X/6-311 ++G (*d*,*p*) energy values for the reactants, intermediates, products, and transition states and are provided in Table S2 in the supplementary material.

3.6 Kinetics

Theoretical determination of the total kinetics of the title reaction is important in order to support the experimental findings and also to provide better insight into the complete reaction features. The initial step of bimolecular association between SiH_3 and H_2O_2 proceeds without any appreciable barrier in the forward direction, and the kinetics of this process therefore require special treatment. We have used variational transition-state theory (VTST) to calculate this barrierless association rate. At low temperatures where enthalpic considerations dominate, the transition state will be *loose*, but at higher temperatures entropic effects constitute a larger contribution to the free energy of activation and we find a *tighter* transition state. In view of the complex temperature dependency due to its variational nature, we have evaluated the rate parameters for the forward (association) reaction at each transition-state structure as a function of temperature along the minimum energy pathway (MEP) in order to identify the variational transition state. The rate constants, $k(T)$, are calculated as a function of temperature from activation enthalpies and entropies at each point along the MEP using canonical transition-state theory and statistical mechanics (Eq. 1) in the temperature range of 250–600 K.

$$k(T) = \sigma(k_b T/h)\exp(\Delta S^{\ddagger}/R)\exp(-\Delta H^{\ddagger}/RT) \quad (1)$$

In Eq. 1, $\Delta S^{\ddagger}$ is the activation entropy, $\Delta H^{\ddagger}$ is the activation enthalpy, k_b is the Boltzmann constant, and h is the Planck constant. Additionally, the apparent rate constants for the unimolecular reactions of the chemically activated species in the $SiH_3 + H_2O_2$ reaction and the branching ratios are obtained using RRKM theory with master equation treatment.

The calculated rate constants are fitted with the following modified three-parameter form of the Arrhenius equation to obtain the elementary rate parameters, A′, E_a, and n

$$k(T) = A'T^n\exp(-E_a/RT) \quad (2)$$

3.6.1 *$SiH_3 + H_2O_2$ association kinetics*

The association between SiH_3 and H_2O_2 forming $SiH_3\cdots H_2O_2$ (**A1**) adduct does not exhibit a distinct transition state due to the absence of a classical saddle point. The VTST calculations are therefore performed to estimate the rate of $SiH_3 + H_2O_2$ association reaction. The minimum energy profile (MEP) for the reaction is determined in order to apply the VTST for the description of the kinetics of the $SiH_3 + H_2O_2$ association reaction. The minimum energy profile for the association of SiH_3 with H_2O_2 along the association coordinate (Si–O) forming the $SiH_3\cdots H_2O_2$ (**A1**) adduct has been constructed at the B2PLYPD/6-311++G(*d*,*p*) level of theory and depicted in Fig. 5. It is also evident from the MEP that the association

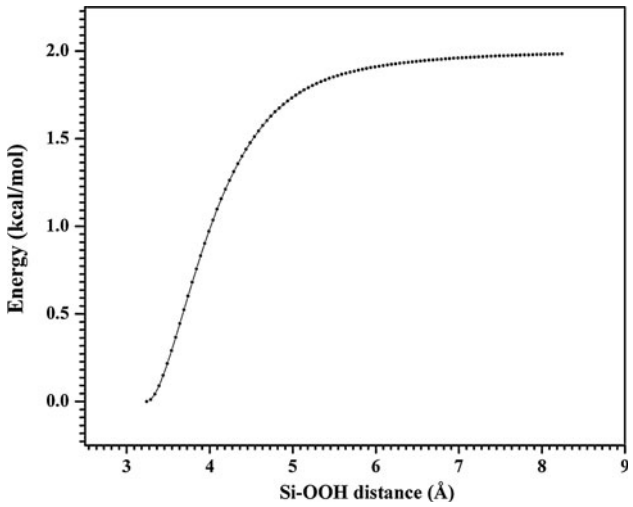

Fig. 5 Relaxed potential energy surfaces for Si–OOH distance (in Å) for the association between SiH_3 and H_2O_2

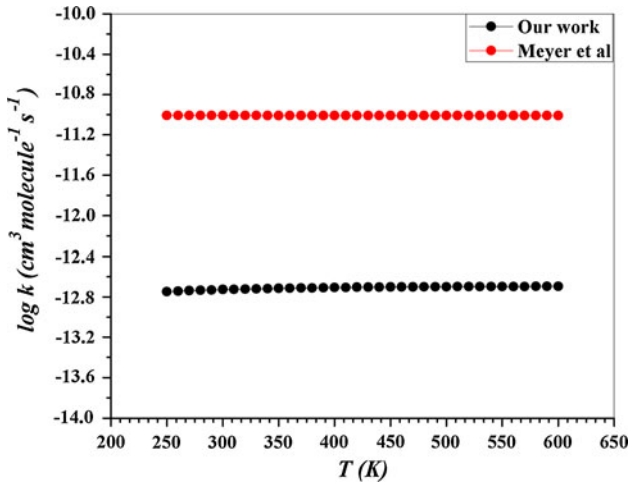

Fig. 6 Comparison of experimental rate constants with variationally computed Arrhenius fitted rate constants for the barrier-less $SiH_3 + H_2O_2$ association reaction

reaction proceeds without a saddle point. The rate constants at each contributing transition-state structures along the MEP have been calculated as a function of temperature in the temperature range of 250–600 K and are plotted in Fig. S2 in the supplementary material. The association reaction is found to be controlled by a very loose transition-state (Si–O = 5.09 Å) structure at 250 K, which is tightened to a Si–O distance 4.94 Å at 600 K. All the variationally computed rate constants are presented in Table S1 in the supplementary material.

The Arrhenius fitted rate constants are presented in Fig. 6 along with the experimentally obtained ones for the association reaction. The empirical rate parameters (A', E_a, n) are fitted to obtain the Arrhenius fitted rate constant for the association reaction, according to standard least square procedure in $k(T)$. The following Arrhenius rate expression for the association part of the reaction is obtained after fitting the rate constants in Eq. 2 where E_a is expressed in kcal mol^{-1}.

$$k(T) = 6.89 \times 10^{-13} T^{-0.163} \exp(-0.22/RT)$$
$$\text{cm}^3 \text{ molecule}^{-1} \text{ s}^{-1} \quad \text{(our work)}$$

Meyer et al., from their experimental study, obtained the following rate expression in the temperature range 298–573 K.

$$k(T) = (9.7 \pm 1.8) \times 10^{-12} T^0 \exp\left[(0.63 \pm 12) \times 10^{-2}/RT\right]$$
$$\text{cm}^3 \text{ molecule}^{-1} \text{ s}^{-1} \quad \text{(Meyer et al.)}$$

The deviation of our calculated rate constants from the experimentally obtained ones may be attributed to the large uncertainty factor associated with the experimental expression of Meyer et al.

3.7 Unimolecular reaction kinetics

The association adduct, **A1**, can undergo further isomerization and dissociation reactions. For the final product formation, we have divided the total unimolecular reaction kinetics study into two successive sections. The first section describes the reactions from the primary adduct, **A1,** and the second section describes the reactions from the secondary adduct, **A3** (refer to PES-I). The title reaction occurs at a finite pressure (0.4 torr in H_2O_2) and the successive unimolecular decompositions can well be at high-pressure limit within the applied temperature window (280–580 K). Therefore, high-pressure limit rate constants are discussed in the following section. Table 3 shows the Arrhenius rate parameters A', n and E_a calculated at finite and infinite pressures.

3.7.1 Unimolecular reactions from A1 ($SiH_3 \cdots H_2O_2$)

From the reaction mechanism studies described in the reaction mechanism section, the unimolecular reaction channels from **A1** can be summarized as

$$\mathbf{A1} \xrightarrow{\text{TS}_{\text{A1-A2}}} \mathbf{A2}(\mathbf{SiH_4 \cdots OOH})$$

$$\mathbf{A1} \xrightarrow{\text{TS}_{\text{A1-A3}}} \mathbf{A3}(\mathbf{SiH_3OH \cdots OH})$$

High-pressure limit rate constants for individual reaction steps from primary complex are calculated as follows:

$$k(T,P) = 3.72 \times 10^{13} T^{-0.56} \exp(-13.13/RT) \text{ s}^{-1}$$
$$(\text{A1} \rightarrow \text{A2})$$

$$k(T,P) = 8.47 \times 10^{08} T^{1.46} \exp(-3.81/RT) \text{ s}^{-1}$$
$$(\text{A1} \rightarrow \text{A3})$$

Apparent rate parameters, A', n, and E_a, for this channel are calculated using a least square analysis on

Table 3 Arrhenius parameters at different pressures for primary and secondary unimolecular reactions

Reactions	Pressure (torr)	A (s^{-1})	E_a (kcal mol^{-1})	n
A1 → A2	0.1	1.65×10^{-18}	6.76	4.77
	0.2	3.08×10^{-08}	9.64	1.48
	0.3	3.31×10^{-12}	8.4	2.78
	0.4	3.94×10^{-06}	10.06	0.83
	P → ∞	3.72×10^{13}	13.13	−0.56
A1 → A3	0.1	8.02×10^{09}	2.11	−1.41
	0.2	1.63×10^{10}	2.12	−1.41
	0.3	2.49×10^{10}	2.12	−1.41
	0.4	3.38×10^{10}	2.13	−1.41
	P → ∞	8.47×10^{08}	3.81	1.46
A3 → P1 + OH + H_2	0.1	1.10×10^{-74}	36.07	23.49
	0.2	1.57×10^{-74}	36.1	23.46
	0.3	1.09×10^{-72}	36.66	22.88
	0.4	2.50×10^{-72}	36.69	22.75
	P → ∞	3.08×10^{12}	65.81	−0.32
A3 → P2 + H_2O	0.1	1.88×10^{-03}	9.78	0.93
	0.2	3.16×10^{-03}	9.74	0.86
	0.3	2.54×10^{-03}	9.64	0.9
	0.4	2.83×10^{-03}	9.6	0.89
	P → ∞	3.10×10^{09}	11.97	1.61
A3 → I1 + H_2O	0.1	1.24×10^{09}	1.98	−1.26
	0.2	1.33×10^{09}	2.02	−1.19
	0.3	1.24×10^{09}	2.05	−1.14
	0.4	1.15×10^{09}	2.06	−1.11
	P → ∞	4.28×10^{08}	4.6	1.48
A3 → I2 + H	0.1	5.34×10^{09}	2.35	−1.44
	0.2	1.87×10^{10}	2.37	−1.51
	0.3	3.73×10^{10}	2.38	−1.55
	0.4	5.88×10^{10}	2.4	−1.57
	P → ∞	6.46×10^{08}	3.84	1.2

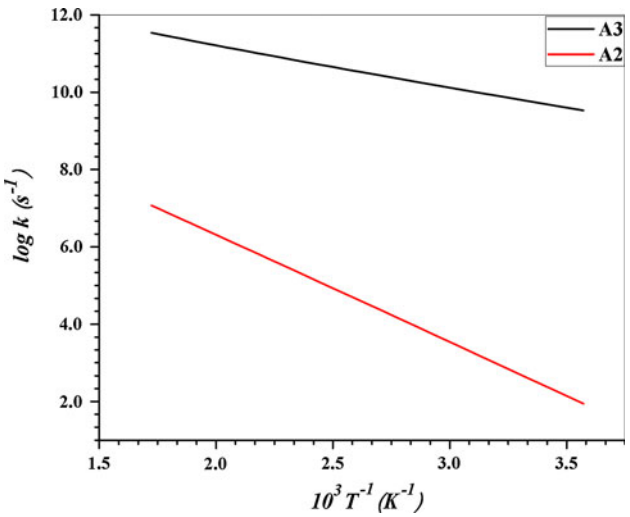

Fig. 7 Arrhenius plot of the calculated high-pressure limit rate constants for different reaction channels from **A1**

the corresponding rate constant and are displayed in Table 3. The logarithms of Arrhenius fitted high-pressure limit rate constants for primary (from **A1**) unimolecular channels are plotted against inverse of temperature in Fig. 7. At the lower temperature range, rate falls off more rapidly for **A2** formation rather than **A3** formation. Small variation is observed in the formation rate for **A3** within the investigated temperature window 280–580 K.

3.7.2 Unimolecular reactions from A3 ($SiH_3OH\cdots OH$)

All unimolecular reactions from the secondary reaction intermediate **A3** can be summarized as follows:

$$\mathbf{A3} \xrightarrow{TS_{A3-P1}} \mathbf{P1}(\mathbf{SiH_2O}) + OH + H_2$$

$$\mathbf{A3} \xrightarrow{TS_{A3-P2}} \mathbf{P2}(\mathbf{SiH_3O}) + H_2O$$

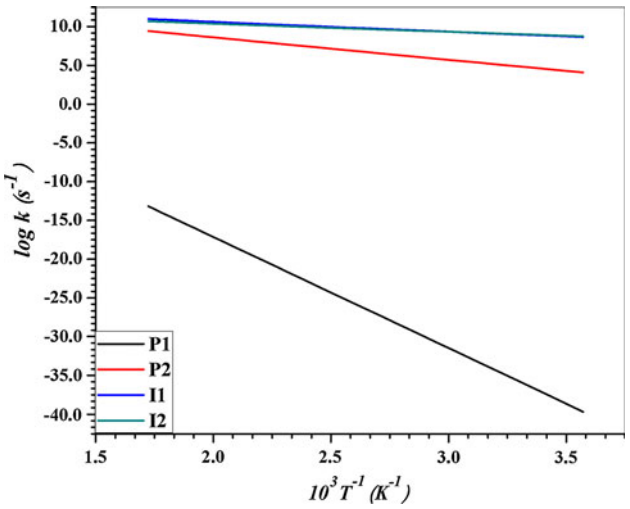

Fig. 8 Arrhenius plot of the calculated high-pressure limit rate constants for different reaction channels from **A3**

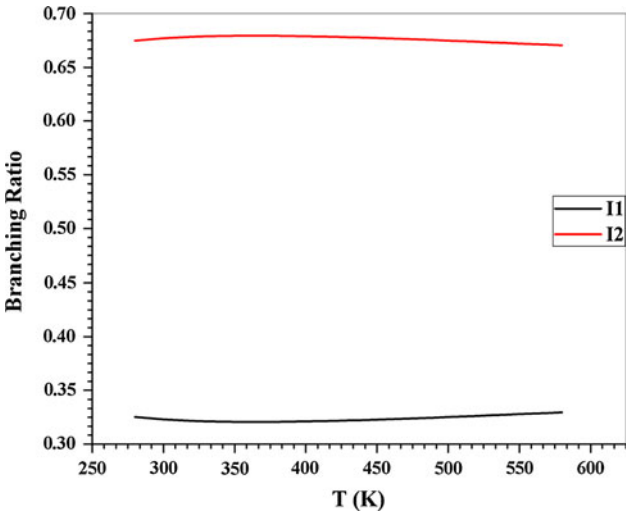

Fig. 9 Branching ratio for channels **A3** → **I1** and **A3** → **I2** at 0.4 torr

$$\mathbf{A3} \xrightarrow{TS_{A3-I1}} \mathbf{I1}(\mathbf{SiH_2OH}) + H_2O$$

$$\mathbf{A3} \xrightarrow{TS_{A3-I2}} \mathbf{I2}(\mathbf{SiH_2(OH)_2}) + H$$

The high-pressure limit rate constants for the individual reaction steps in the above scheme are calculated to be

$$k(T,P) = 3.08 \times 10^{12} T^{-0.32} \exp(-65.81/RT)\ \mathrm{s}^{-1}$$
$$(\mathrm{A3} \rightarrow \mathrm{P1}(\mathrm{SiH_2O}) + \mathrm{OH} + \mathrm{H_2})$$

$$k(T,P) = 3.10 \times 10^{09} T^{1.61} \exp(-11.97/RT)\ \mathrm{s}^{-1}$$
$$(\mathrm{A3} \rightarrow \mathrm{P2}(\mathrm{SiH_3O}) + \mathrm{H_2O})$$

$$k(T,P) = 4.28 \times 10^{08} T^{1.48} \exp(-4.60/RT)\ \mathrm{s}^{-1}$$
$$(\mathrm{A3} \rightarrow \mathrm{I1}(\mathrm{SiH_2OH}) + \mathrm{H_2O})$$

$$k(T,P) = 6.46 \times 10^{08} T^{1.2} \exp(-3.84/RT)\ \mathrm{s}^{-1}$$
$$(\mathrm{A3} \rightarrow \mathrm{I2}(\mathrm{SiH_2(OH)_2}) + \mathrm{H})$$

The Arrhenius rate parameters, A', n, and E_a, for these channels are calculated and are summarized in Table 3. The logarithm of high-pressure limit rate constants is plotted against inverse of temperature in Fig. 8. It is observed that the formation of **P2** has a comparable rate with **I1** and **I2** formation and the rate variation of which is not significant within 280–580 K, whereas the formation rate for **P1** varies rapidly with temperature within the same temperature range.

3.8 Product branching ratios

Based on the calculated rate parameters, it is now our goal to evaluate the product branching ratios for various unimolecular reaction channels from primary (**A1**) and secondary (**A3**) reaction intermediates for the major product channels at 0.4 torr. No further attempt has been made in the present study toward the kinetics evaluation of the unimolecular reactions after **A3**, and therefore, the major reaction channels are qualitatively explained with the help of primary and secondary unimolecular branching ratios.

The isomerization of **A1** to **A3** has a very high branching ratio (~1) over the isomerization of **A1** to **A2**, which is associated with negligible branching ratio (2.26×10^{-17}). Therefore, the isomerization to **A3** is taken as the exclusive channel from **A1**.

Among the four possible channels from **A3**, there are two competitive channels yielding **I1** and **I2** through H_2O-loss and H-loss, respectively. The product branching ratios for the two channels producing **P1** (1.09×10^{-49}) and **P2** (8.58×10^{-14}) are negligibly small compared to **I1** (0.32) and **I2** (0.67) product channels. The rate constant for **I1** channel is ten times lower than the competing **I2** channel near 300 K and at 0.4 torr. The temperature variations of the product branching ratios for these two competing channels are presented in Fig. 9. Therefore, primary unimolecular decomposition channel forming $SiH_3OH\cdots OH$ (**A3**) followed by SiH_2OH (**I1**) and $SiH_2(OH)_2$ (**I2**), and finally, SiO is associated with exclusively high branching ratio. In contrast, the successive decomposition of **A3** to form OH (**A3** → $\mathbf{SiH_2O} + \mathbf{OH} + \mathbf{H_2}$) is associated with negligibly low branching ratio. Therefore, previous explanation regarding major and minor product channels yielding SiO and OH, respectively, runs parallel with the branching ratio calculation as well.

4 Conclusions

In the present theoretical reaction mechanism study followed by kinetics calculation, we have explored all the

features of major and minor production channels of the elementary reactions of the SiH_3 radical with H_2O_2 on its doublet PES. The VTST calculations on the barrier-less association followed by RRKM master equation calculation on the unimolecular reactions have been performed to elucidate the experimental observation and also to justify our prediction for a new major channel toward SiO production. The barrier-less association between SiH_3 and H_2O_2 gives rise to the adduct **A1** through which the occurrence of one previously assumed channel (forming **A2**) can be explained. This association process is found to be exothermic and the adduct, **A1**, in a parallel highly exothermic reaction channel, produces **A3**, which is proved to be the key intermediate of the other previously assumed channels (forming **P1** and **P2**) and also to the channels forming **I1** and **I2** which are not yet detected experimentally. The low-barrier **I1** and **I2** formation channels are found to be highly exothermic, which is expected to rule out the direct decomposition of **A3** to SiH_3OH (**P2a**) and OH. Our theoretical calculations enable us to solve the long-standing confusion about the major product channel of the title reaction. Also, our theoretical work has firmly established that the hydrogen-loss pathway (**I2** forming pathway) is the major product channel leading to SiO deposition and is in agreement with the work of Meyer et al. that the OH producing channel is very minor. A subsequent RRKM calculation and thereby the branching ratio analysis have also clarified the dominance of **I2** over its competitive counterpart **I1** and have also eliminated the occurrence of the previously assumed channels producing $SiH_4\cdots OOH$ (**A2**), SiH_2O (**P1**), and SiH_3O (**P2**). Therefore, combining the present result with the available experimental findings, it is concluded that the predicted H-loss pathway is the major decomposition channel of the title reaction to produce SiO rather than the OH producing one.

Acknowledgments K.S. is very much grateful to the Council of Scientific and Industrial Research (CSIR), Government of India, for providing him research fellowships. A.K.D. is grateful to the Council of Scientific and Industrial Research (CSIR), Govt. of India, for a research grant under scheme number: 03(1168)/10/EMR-II. Thanks are due to Mr. Debasish Mandal for his assistance and helpful discussions. We are thankful to Prof. Vladimir Mokrushin for helping us on time-dependent RRKM master equation simulation with ChemRate.

References

1. Jasinski JM, Meyerson BS, Scott BA (1987) Ann Rev Phys Chem 38:109
2. Jasinski JM, Gates SM (1991) Acc Chem Res 24:9
3. Pankove JI (ed) (1984) Semiconductors and Semimetals, vol 21A. Academic Press, New York
4. Jensen KF (1989) Adv Chem Ser 221:199
5. Blankenship MG, Deneka CW (1982) IEEE J Quantum Electron QE-18:1418
6. Suga S, Koda S (1988) Jpn J Appl Phys 27:L1966
7. Hartman JR, Famil-Ghiriha J, Ring MA, O'Neal HE (1987) Combust Flame 68:43
8. Koda S (1992) Prog Energy Combust 18:513
9. Koda S, Fujiwara O (1986) In: Proceedings of the 21st international symposium on combustion, The Combustion Institute, Pittsburgh, p 1861
10. Chung SL, Tsai MS, Lin HD (1991) Combust Flame 85:134
11. Kondo S, Tokuhashi K, Nagai H, Iwasaki M, Kaise M (1995) Combust Flame 101:170
12. Kondo S, Tokuhashi K, Nagai H, Iwasaki M, Kaise M (1994) Combust Flame 97:296
13. McLain AG, Jachimowski CJ, Rogers RC (1983) NASA TP-2114
14. Jachimowski CJ, McLain AG (1983) NASA TP-2129
15. Koda S, Fujiwara O, Ohnishi T (1986) Combust Flame 65:121
16. Koda S, Fujiwara O (1988) Combust Flame 73:187
17. Tokuhashi K, Horiguchi S, Urano Y, Iwasaka M, Ohtani H, Kondo S (1990) Combust Flame 82:40
18. Britten JA, Tong J, Westbrook CK (1990) In: Twenty-third symposium (international) on combustion, The Combustion Institute, Pittsburgh, p 195
19. Fukutani S, Uodome Y, Kunioshi N, Jinno H (1991) Bull Chem Soc Jpn 64:2328
20. Zachariah MR, Semerjian HG (1989) AIChE J 35:2003
21. Zachariah MR (1990) In: Messing G (ed) Ceramic powder science III, vol 12, p 283
22. Chesovnikov SA, Krasnoperov LN (1990) Kinet Catal 31:1125
23. Kushner MJ (1987) J Appl Phys 62:2803
24. Robertson R, Gallagher A (1986) J Appl Phys 59:3402
25. Gallagher A (1988) J Appl Phys 63:2406
26. Itabashi N, Kato K, Nishiwaki N, Goto T, Yamada C, Hirota E (1989) Jpn J Appl Phys 28:L325
27. Krasnoperov LN, Chesnokov EN, Panfilov VN (1984) Chem Phys 89:297
28. Yamada C, Hirota E (1986) Phys Rev Lett 56:923
29. Slagle IR, Bernhardt JR, Gutman D (1988) Chem Phys Lett 149:180
30. Sugawara K, Nakanaga T, Takeo H, Matsumura C (1989) Chem Phys Lett 157:309
31. Koshi M, Miyoshi A, Matsui H (1991) J Phys Chem 95:9869
32. Quandt R, Hershberger JF (1993) Chem Phys Lett 206:355
33. Chasovnikov SA, Krasnoperov LN (1987) Chim Fiz 6:956
34. Kondo S, Tokuhashi K, Nagai H, Takahashi A, Kaise M, Sugie M, Aoyagi M, Mogi K, Minamino S (1997) J Phys Chem A 101:6015
35. Darling CL, Schlegel HB (1994) J Phys Chem 98:8910
36. Murakami Y, Koshi M, Matsui H, Kamiya K, Umeyama H (1996) J Phys Chem 100:17501
37. Koshi M, Nishida N, Murakami Y, Matsui H (1993) J Phys Chem 97:4473
38. Loh SK, Beach DB, Jasinski JM (1990) Chem Phys Lett 169:55
39. Marshall P (1993) Chem Phys Lett 201:493
40. Matsumoto K, Koshi M, Okawa K, Matsui H (1996) J Phys Chem 100:8796
41. Loh SK, Jasinski JM (1991) J Chem Phys 95:4914
42. Seetula JA, Feng Y, Gutman D, Seakins PW, Pilling JM (1991) J Phys Chem 95:1658
43. Raghunath P, Lin MC (2010) J Phys Chem A 114:13353
44. Meyer JP, Hershberger JF (2003) J Phys Chem A 107:5963
45. Roland RP, Anderson RW (2001) Chem Mater 13:2501
46. Roland RP, Bolle M, Anderson RW (2001) Chem Mater 13:2493
47. Zhao Y, Truhlar DG (2008) Theor Chem Acc 120:215
48. Schwabe T, Grimme S (2007) Phys Chem Chem Phys 9:3397
49. Krishnan R, Binkley JS, Seeger R, Pople JA (1980) J Chem Phys 72:650

50. Curtiss LA, Redfern PC, Raghavachari K (2007) J Chem Phys 127:124105
51. Montgomery JA Jr, Frisch MJ, Ochterski JW, Petersson GA (1999) J Chem Phys 110:2822
52. Gonzales C, Schlegel HB (1989) J Chem Phys 90:2154
53. Gonzales C, Schlegel HB (1990) J Phys Chem 94:5523
54. Frisch MJ, Trucks GW, Schlegel HB, Scuseria GE, Robb MA, Cheeseman JR, Scalmani G, Barone V, Mennucci B, Petersson GA, Nakatsuji H, Caricato M, Li X, Hratchian HP, Izmaylov AF, Bloino J, Zheng G, Sonnenberg JL, Hada M, Ehara M, Toyota K, Fukuda R, Hasegawa J, Ishida M, Nakajima T, Honda Y, Kitao O, Nakai H, Vreven T, Montgomery JA Jr, Peralta JE, Ogliaro F, Bearpark M, Heyd JJ, Brothers E, Kudin KN, Staroverov VN, Keith T, Kobayashi R, Normand J, Raghavachari K, Rendell A, Burant JC, Iyengar SS, Tomasi J, Cossi M, Rega N, Millam JM, Klene M, Knox JE, Cross JB, Bakken V, Adamo C, Jaramillo J, Gomperts R, Stratmann RE, Yazyev O, Austin AJ, Cammi R, Pomelli C, Ochterski JW, Martin RL, Morokuma K, Zakrzewski VG, Voth GA, Salvador P, Dannenberg JJ, Dapprich S, Daniels AD, Farkas O, Foresman JB, Ortiz JV, Cioslowski J, Fox DJ (2010) Gaussian 09, ReVision B.01. Gaussian Inc., Wallingford
55. Nicolaides A, Rauk A, Glukhovtsev MN, Radom L (1996) J Phys Chem 100:17460
56. Afeefy HY, Liebman JF, Stein SE (2005) Neutral thermochemical data. In: Linstrom PJ, Mallard WG (eds) NIST chemistry webbook, NIST Standard Reference Database Number 69. National Institute of Standards and Technology, Gaithersburg, MD. (http://webbook.nist.gov)
57. Duncan WT, Bell RL, Truong TN (1998) TheRate: Program for ab initio direct dynamics calculations of thermal and vibrational-state selected rate constants. J Comput Chem 19:1039 (http://cse-online.net)
58. Silva GD, Bozzelli JW (2008) J Phys Chem A 112:3566
59. Silva GD, Hamdan MR, Bozzelli JW (2009) J Chem Theory Comput 5:3185
60. Mandal D, Mondal B, Das AK (2011) Phys Chem Chem Phys 13:4583
61. Klippenstein SJ (1992) J Chem Phys 96:367
62. Klippenstein SJ, Marcus RA (1987) J Chem Phys 87:3410
63. Wardlaw DM, Marcus RA (1984) Chem Phys Lett 110:230
64. Wardlaw DM, Marcus RA (1985) J Chem Phys 83:3462
65. Mokrushin V, Bedanov V, Tsang W, Zachariah M, Knyazev V (2009) ChemRate Version 1.5.8. National Institute of Standards and Testing, Gaithersburg, MD
66. Eckart C (1930) Phys Rev 35:1303
67. Lee TJ, Taylor PR (1989) Int J Quantum Chem S23:199
68. Rienstra-Kiracofe JC, Allen WD, Schaefer HF III (2000) J Phys Chem A 104:9823
69. Peiro-Garcia J, Nebot-Gil I (2003) Chem Phys Chem 4:843
70. Peiro-Garcia J, Nebot-Gil I (2003) J Comput Chem 24:1657
71. Martinez-Avila M, Peiro-Garcia J (2003) Chem Phys Lett 370:313
72. Lambert N, Kaltsoyannis N, Price SD, Zabka J, Herman Z (2006) J Phys Chem A 110:2898
73. Miller SR, Schultz NE, Truhlar DG, Leopold DG (2009) J Chem Phys 130:024304
74. Zachariah MR, Tsang W (1995) J Phys Chem 99:5308
75. Doncaster AM, Walsh R (1981) Int J Chem Kinet 13:503
76. Chase MW Jr (1998) NIST-JANAF thermochemical tables, 4th edn. J Phys Chem Ref Data Monogr 9:1–1951
77. Gronert S, O'Hair RAJ, Prodnuk S, Sulzle D, Damrauer R, DePuy CH (1990) J Am Chem Soc 112:997